Nuclear Instruments and Methods in Physics Research A 377 (1996) 298–311

NUCLEAR INSTRUMENTS & METHODS IN PHYSICS RESEARCH
Section A

ELSEVIER

Analysis of trapping effects on charge transfer in proton irradiated pn-CCDs

Norbert Meidinger[a,*,1] Lothar Strüder[a], Peter Holl[b], Heike Soltau[b], Christoph v. Zanthier[b]

[a] Max-Planck-Institut für extraterrestrische Physik, Giessenbachstraße, D-85740 Garching, Germany
[b] KETEK GmbH, Am Isarbach 30, D-85764 Oberschleißheim, Germany

Abstract

A new type of Charge Coupled Device, a pn-CCD, was developed for the European Photon Imaging Camera (EPIC) on the X-ray Multi Mirror (XMM) satellite mission of the European Space Agency. The detector for fast X-ray imaging and spectroscopy uses pn-junctions instead of the traditional MOS-gates. To prove the detector radiation hardness, four pn-CCDs were irradiated with 10 MeV-protons of fluences ranging from 6.0×10^8 up to $6.5 \times 10^9\ \mathrm{cm}^{-2}$. The equivalent 10 MeV-proton fluence is estimated at $3.6 \times 10^8\ \mathrm{cm}^{-2}$ for the ten year satellite mission. It turned out that the Charge Transfer Efficiency is the most irradiation sensitive detector parameter. The trap dependent charge transfer is described by a Monte Carlo simulation model which considers all relevant parameters. The simulations agree well with the results of the measurements. This method was also applied for defect analysis. The predominant radiation induced defect type was identified as a vacancy-oxygen trap, called A-centre$^{(0/-)}$. The result is confirmed by Deep Level Transient Spectroscopy (DLTS) measurements and annealing experiments.

1. Introduction

A pn-CCD detector [1,2] will be used as main focal plane instrumentation for one of three independent Wolter telescopes in ESA's cornerstone XMM satellite mission [3]. The ten year X-ray astronomy mission is planned to be launched in 1999.

1.1. Detector

Design, fabrication and test of the pn-CCD detector are carried out in the semiconductor laboratory of the Max-Planck-Institute. The sensitive area of the pn-CCD detector system is 36 cm^2 consisting of 12 single subsystems [1,2]. Each of these single units has 64 parallel transfer channels terminated with an integrated input-JFET for signal amplification and a JFET reset switch. A transfer channel consists of 200 pixels with a size of 150 μm × 150 μm. In contrast to the common Charge Coupled Device with MOS-gates for the charge transfer, the pn-CCD uses reverse biased strip diodes. Depletion of the 280 μm thick detector is accomplished with the large area reverse biased pn-diode at the opposite wafer surface. It acts simultaneously as radiation entrance window (Fig. 1). The pn-CCD concept has the advantage of a high photon detection efficiency (>90% in the energy range from 500 eV to 10 keV) combined with a high energy resolution (e.g. FWHM = 140 eV at 140 K for Mn-K$_\alpha$ (5893 eV)) and a fast readout (4.5 ms). The position resolution of 3.5 arcsec in two dimensions of the detector in the satellite mission is matched to the angular resolution of the telescope (≈20 arcsec). The basic concept of the pn-CCD

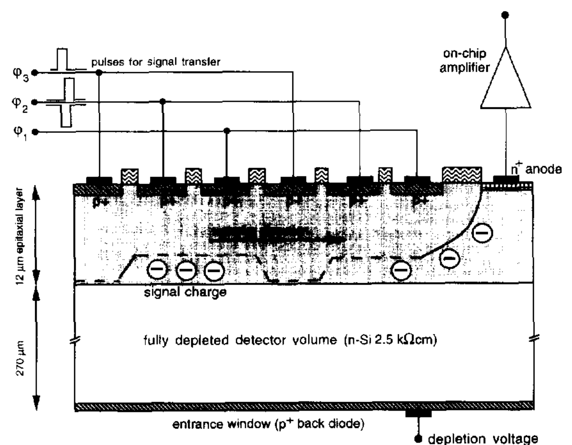

Fig. 1. A schematic cross section through the fully depleted pn-CCD along a transfer channel. The X-ray photons are entering from the homogeneous backside. The potential minimum for signal electrons is about 10 μm below the register surface. An appropriate voltage pulse sequence at the three registers φ1, φ2 and φ3 causes the signal electrons to move to the anode [1].

* Corresponding author.
[1] Postal address: MPI Halbleiterlabor, Paul-Gerhardt-Allee 42, 81245 München, Germany.

0168-9002/96/$15.00 Copyright © 1996 Elsevier Science B.V. All rights reserved
PII S0168-9002(96)00255-0

detector for XMM is described in Refs. [1,3] and its present performance is given in Ref. [2].

1.2. Transfer region and timing scheme

The three phase detector design and the timing scheme result in six successive and separate storage regions per pixel during the transfer to the anode; three below the shift registers $\varphi 1$, $\varphi 2$, $\varphi 3$ and three between the shift registers. The volume of a storage location is in the order of 10^2 μm^3. The simulation in Fig. 2 shows the electric potential in a depth of 10 μm below the shift registers. In addition, the time dependent change of the potential is described when shifting the charge from below $\varphi 3$ towards the anode, between $\varphi 3$ and $\varphi 2$.

The timing scheme for the pn-CCD operation consists of the integration time Δt_i, the readout time Δt_r and the transfer time Δt_s (Fig. 3). The time Δt_c for taking one image with n rows is called cycle time:

$$\Delta t_c = \Delta t_i + n \times (5 \times \Delta t_s + \Delta t_r) . \quad (1)$$

The charges which are generated during the integration time (tens of milliseconds) are stored under the shift register $\varphi 1$. After the integration time the signals are shifted row by row towards the anode. The charge packets stay one third of the shift register pulse width Δt_s (hundreds of nanoseconds) at each of the five storage locations during the shift of one pixel. Afterwards they are stored again under the shift register $\varphi 1$ for the readout time Δt_r (tens of microseconds). This time is needed for signal processing of each row (64 pixel) in the preamplifier.

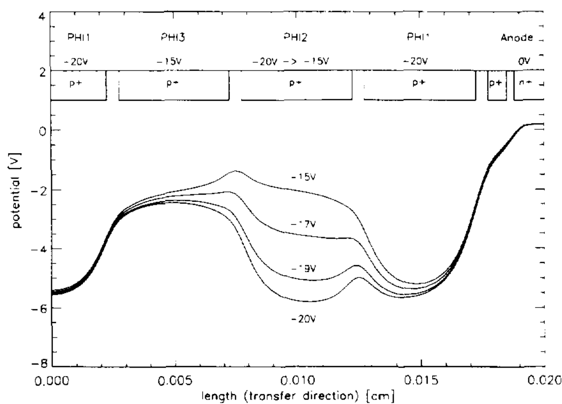

Fig. 2. Simulation of transfer potentials in a pn-CCD with TOSCA program code [4]. The potential at the transfer depth of 10 μm is shown for charge storage under shift register $\varphi 3$ ($\varphi 2 = -20$ V). Also depicted is the potential change for the transfer to the region between $\varphi 3$ and $\varphi 2$ ($\varphi 2 = -20\ \mathrm{V} \rightarrow -15$ V), at which the electrons are gathered for the next period of time ($\varphi 2 = -15$ V).

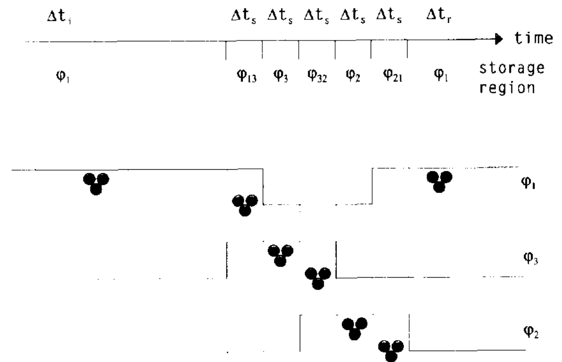

Fig. 3. Timing scheme and storage regions of the pn-CCD. The signal charge is stored during transfer in six successive regions; below the three shift registers $\varphi 1$, $\varphi 2$, $\varphi 3$ and between them. The storage time below shift register $\varphi 1$ is determined by the integration time Δt_i and the readout time Δt_r for each row (64 pixel simultaneously) respectively. The signal charges remain one third of the shift register pulse width Δt_s at the other five storage places each during the transfer. The fast transfer from one storage location to the next occurs within 10 ns.

1.3. Traps and charge transfer

Silicon lattice defects with an energy level in the bandgap can act as trapping centers (traps). They capture electrons (respectively holes) and release them after a certain time into the conduction band (valence band respectively). If the emission time is much longer compared to the storage time, a trapped signal electron reaches the anode later than the signal charge packet. The mean relative loss of signal charges per pixel transfer is called Charge Transfer Inefficiency (CTI). It is related to the Charge Transfer Efficiency by CTE = 1 − CTI. A constant Charge Transfer Efficiency per pixel transfer results in a signal S_n after n transfers:

$$S_n = \mathrm{CTE}^n \times S_0 \qquad (n = 1, 2, 3, \ldots) , \quad (2)$$

with S_0 the number of generated signal electrons. The absolute charge loss for transfer #n is calculated by $\mathrm{CTI} \times S_{n-1}$.

1.3.1. Energy resolution

Without charge transfer losses we would obtain a CTE value of one. The real CTE is smaller and can degrade the energy resolution for two reasons. Firstly, the CTE has to be determined to correct the charge losses according to Eq. (2). The CTE however is dependent on different conditions like device operation, temperature, X-ray energy and intensity and radiation exposure. Secondly, it represents a contribution to noise, called transfer noise. The square of this noise contribution is dependent on the Charge Transfer Efficiency, the X-ray energy and the number of transfers to

the anode [5]. The sum of the squares of the single noise sources (transfer noise, Fano noise, electronic noise, etc.) determines the spectral resolution.

1.3.2. Time constants for electron capture and emission

According to the Shockley–Read–Hall recombination-generation theory the electron trap occupation and depopulation in a pn-CCD can be described by Refs. [6–9]:

$$\frac{dn_t^+}{dt} = -\frac{n_t^+}{\tau_c} + \frac{n_t - n_t^+}{\tau_e}, \quad (3)$$

with a time constant τ_c for electron capture into an empty trap:

$$\tau_c = \frac{1}{\sigma_c v_{th} n_s}, \quad (4)$$

and a time constant τ_e for electron emission out of an occupied trap:

$$\tau_e = \frac{1}{\sigma_c X_n v_{th} N_c} \exp\left(\frac{E_c - E_t}{kT}\right), \quad (5)$$

with

n_t^+ = density of empty traps at the time t,
n_t = total density of traps,
σ_c = electron capture cross section,
v_{th} = average thermal velocity of electrons,
n_s = free electron density,
X_n = entropy change factor by electron emission,
N_c = effective density of states in the conduction band,
$E_c - E_t$ = energy level of the electron trap referring to the conduction band edge,
k = Boltzmann constant,
T = absolute temperature.

It is obvious from Eq. (5) that the emission time is very dependent on the energy level of the trap and varying with the temperature of the device over a wide range of values. Typical electron capture and emission times are shown in Figs. 4 and 5.

Traps can be present in the silicon substrate material or are produced during device fabrication, especially during doping by implantations. Another possibility for trap generation is radiation exposure of silicon.

1.4. Radiation hardness of pn-CCDs

The main radiation fluxes to detectors in the satellite orbits consist of protons, electrons and photons. Their energy is deposited in the devices mainly by ionization.

1.4.1. Surface damage

Radiation exposure of MOS-structures leads to surface damage, i.e. positive charge buildup in the oxide and creation of interface states. This results in a flatband voltage shift which affects the charge transfer. This is

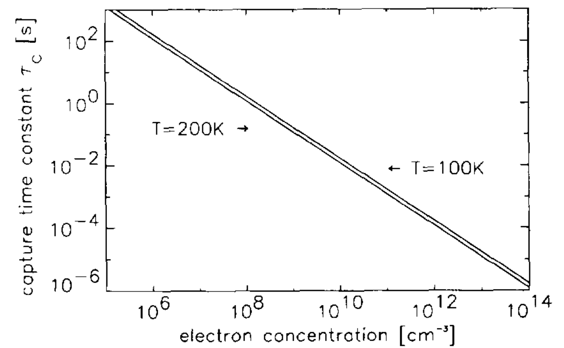

Fig. 4. Capture time constant τ_c versus electron concentration for a capture cross section $\sigma_c = 1 \times 10^{-15}\ cm^2$ and two different temperatures of 100 K and 200 K. The transfer from one confined storage region to the next one needs a time in the order of 10 ns. The electron density is lower than $5 \times 10^{12}\ cm^{-3}$ during this shift over the relatively large distance of 25 μm. We conclude from the figure that the capture time constant τ_c (>10 μs) is a few orders of magnitude higher than the time which the signal charges remain between the single storage places (≈10 ns). Trapping between the storage regions is therefore negligible compared to trapping in the storage regions.

avoided in the pn-CCD by the usage of pn-junctions for charge storage and transfer. In addition, the transfer depth of about 10 μm is far away from the surface compared to MOS-CCDs with a transfer depth of typically 0.5 μm.

1.4.2. Bulk damage

Trap formation: An incident particle or a high energy photon can displace a silicon atom of the bulk from its lattice position. Protons have to exceed a threshold of 100 eV for the formation of a vacancy and a silicon interstitial atom, while photons need an energy of at least 170 keV [10]. Interactions of vacancies or interstitials with impurity atoms, or vacancies with each other, can form stable trapping centers. Especially vacancy-phosphorus defect formation (E-centre) after electron or proton irradia-

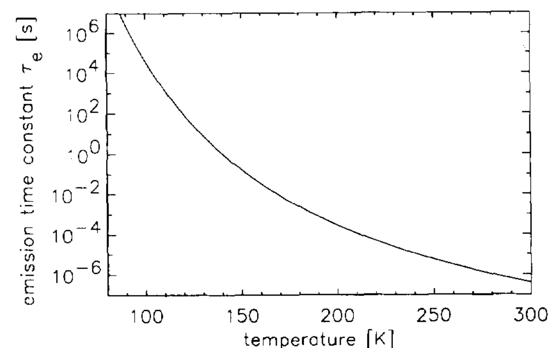

Fig. 5. Emission time constant τ_e versus temperature for a trap with $E_t = E_c - 0.30$ eV, $\sigma_c = 1 \times 10^{-15}\ cm^2$, $X_n = 1$.

tion, is well-known to be induced in phosphorus doped silicon. Examples for the generation of E-centres in MOS-CCDs are given in Refs. [11–13]. The phosphorus concentration in the transfer region of the pn-CCD is only $1 \times 10^{14}\,cm^{-3}$. Therefore the probability of E-centre formation by radiation exposure is lower in the pn-CCD compared to the MOS-CCD in which the phosphorus concentration is at least $10^{16}\,cm^{-3}$.

Trapping between storage regions: The signal charges are shifted by high and far-ranging drift fields (0.1–1 kV/cm, see Fig. 2). The very fast transfer from one confined storage location to another, is in the order of ten ns. The electron density is lower than $5 \times 10^{12}\,cm^{-3}$ during the transfer over the distance of 25 μm to the next storage place. The time for the transfer to the next storage region is a few orders of magnitudes shorter than the capture time constant τ_c of a trap in that area (according to Eqs. (3), (4), see Fig. 4). For this reason we conclude that charge losses are negligible between the storage regions.

Range of storage potential: If a trapped signal electron is released while its charge packet is already transferred to the next storage region, it drifts again to the signal packet. This is accomplished by the far-ranging high drift fields of the storage potentials in the pn-CCD pixels (see Fig. 2). Thereby the signal charge losses are kept small for temperatures with emission time constants τ_e up to the order of the storage times.

2. Irradiation experiment

2.1. Irradiation

The amount of nonionizing energy loss which results in bulk damage, is higher for protons than for electrons or photons of the same energy. The energy loss per unit length increases for lower proton energies. The range of protons with an energy of 10 MeV is still about 700 μm in silicon. For that reason, 10 MeV protons are used as a standard irradiation source to study both, displacement and ionization damage for devices operated in orbit. They deposit an average energy of 2.4 MeV for vertical incidence to the pn-CCD.

Protons of that energy from the TANDEM accelerator of the University and the Technical University of Munich were scattered in a thin gold foil in a vacuum chamber. The intensity and energy of the Rutherford scattered protons is dependent on the scattering angle and the thickness of the gold foil. By mounting the devices under different angles with respect to the beam, it was possible to expose simultaneously several devices to different fluxes in the same irradiation run (see Table 1). Four pn-CCDs and ten large area test diodes of the CCD wafers were irradiated in three runs. The irradiated pn-CCDs were test devices of fabrication #6 of 1993. They possessed 60 pixels per transfer channel. The pn-CCDs were irradiated from the backside (photon entrance window) at room temperature. All relevant DC operating voltages were applied. Half of the 64 pn-CCD channels were shielded by a 1 mm thick iron plate. The effects of irradiation could therefore be observed by comparison of irradiated and shielded transfer channels. Identical operating conditions (in particular concerning temperature) are thereby guaranteed. A description of the experiment is given in Ref. [15].

2.2. Performance degradation

2.2.1. Device test

After the proton irradiation the pn-CCDs were tested in the laboratory in a vacuum test facility. It has a ^{55}Fe X-ray source at disposal with Mn-$K_{\alpha,\beta}$ lines (5.894 eV, 6.489 eV). Measurements with Al-K_α (1.486 eV) and Cu-K_α (8.040 eV) photons from an X-ray tube with variable photon intensities completed the tests. X-rays of this energy cannot transfer the minimum displacement energy of about 15 eV to a silicon lattice atom because of the low mass of the generated photo-electron. The trap concentration remained therefore constant during the measurements. The pn-CCDs were irradiated homogeneously with photons (flat field) to study all pixels of the devices with the same photon flux. The detector was cooled by a cryogenic pump allowing a wide range of operating temperatures from 60 K to 250 K.

The increase in bulk leakage current turned out to be not significant at the low operation temperatures (<200 K) planned for the detector on the satellite.

Table 1
The four pn-CCDs in the irradiation experiment, proton fluences, energy deposition in the device per proton (after passing through the scattering foil), dose in transfer depth (calculated with Monte Carlo program code TRIM90 [14]) and duration of proton exposure. For the run with device C6-23-12 a thicker scattering foil was used which results in a higher energy deposition in the device.

CCD-id	Proton fluence [cm^{-2}]	$\Delta E/p$ [MeV]	Dose in transfer depth [krad]	Irradiation time [h]
C6-21-12	6.0×10^{8}	2.4	0.40	5.5
C6-21-3	1.5×10^{9}	2.4	1.0	5.5
C6-28-3	2.6×10^{9}	2.4	2.0	4
C6-23-12	6.5×10^{9}	3.3	6.7	14.5

2.2.2. Scatterplot

The measured signal heights of X-rays versus the number of pixel transfers towards the anode are described by a scatterplot. Fig. 6 shows it for the irradiated channels of device C6-23-12. The operating temperature was 124 K. The upper curve shows the signal of the leading pixel, the two lower lines describe the electrons in the first and second successive pixels.

2.2.3. CTE dependence on temperature and proton flux

CTE turned out to be approximately constant for each pixel transfer of the irradiated and shielded channels respectively.

The crucial difference between shielded and irradiated channels was a temperature dependent degradation of CTE. Fig. 7 shows the CTE degradation versus operating temperature for different proton irradiation fluences. A proton fluence dependent CTE degradation could be observed at a temperature around 120 K. Furthermore a second CTE minimum was found at temperatures around 190 K (see Fig. 8). This minimum is already present in the non irradiated detectors. It is appreciably changed only for the highest irradiation level (see Fig. 7). The observed temperature dependence is characteristic for traps (see Section 4). This shows that Charge Transfer Efficiency in the pn-CCD is mainly determined by traps and not by bad timing, device design or operation.

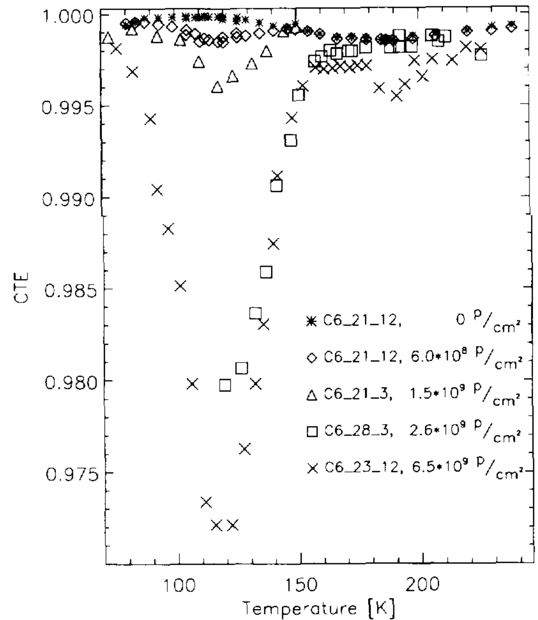

Fig. 7. Temperature dependence of CTE on different 10 MeV-proton fluences to the pn-CCDs. The worst degradation arises at a temperature of about 120 K. The values were measured with Mn-K X-rays with a flux of about 500 photons/cm^2 s, an integration time Δt_i of 76 ms, a readout time per row (64 pixel) Δt_r of 59 μs and a storage time Δt_s during charge transfer of 900 ns.

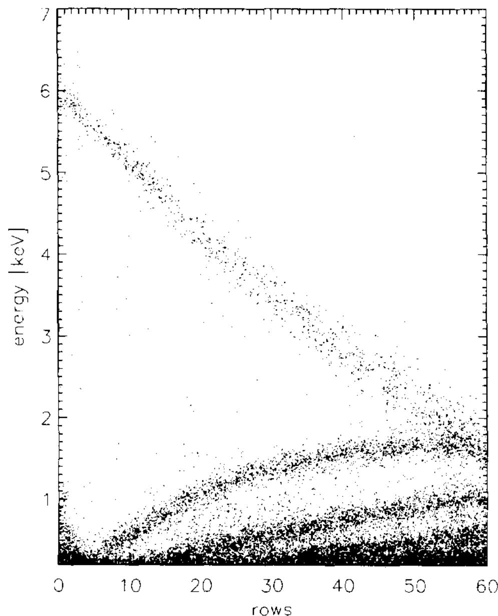

Fig. 6. Scatterplot, i.e. single Mn-$K_{\alpha,\beta}$ signals vs number of pixel transfers to anode. It corresponds to the pn-CCD channels which were exposed to the highest proton fluence of 6.5×10^9 cm^{-2}. The operation temperature of 124 K is close to the CTE minimum. The upper curve shows the signal amplitudes of the leading pixels. The first and second successive pixels collect most of the trapped electrons resulting in the two curves at the bottom. The signals between the curves (with respect to the ordinate) are the fractions of signal charge packets which are split up into two or more pixels (split events). Furthermore we have a contribution of out-of-time events which are incident not during integration time but during the transfer. They are assigned thereby to wrong pixels and their signals are spread along the abscissa in the scatterplot.

2.2.4. CTE dependence on photon energy

The dependence of CTE on photon energy was studied with Mn-K_α (5.894 eV) and Al-K_α (1.486 eV) photons. The temperature scans of CTE are shown in Fig. 8 and Fig. 9 respectively. The relative charge loss CTI = 1 − CTE is obviously higher for the lower photon energy. The absolute charge loss however, is lower than for Mn-K_α X-rays.

2.2.5. CTE dependence on photon flux

A variation over a wide range of fluxes is shown in Fig. 10 for Cu-K_α X-rays. CTE increases appreciably only for high photon fluxes.

The CTE dependence on two different Al-K_α intensities (for irradiated and shielded channels respectively) is shown in Fig. 9. The CTE increase for the higher photon flux is not significant in these measurements.

2.2.6. CTE dependence on storage time

The storage time of the electrons is mainly determined by Δt_s (five times per row) compared with the readout time

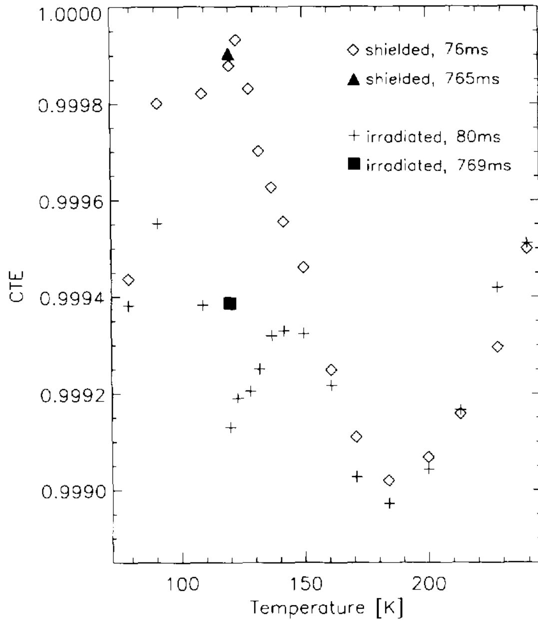

Fig. 8. CTE dependence on temperature for pn-CCD C6-21-12. Half of the channels of the device were exposed to the lowest proton fluence of $6.0 \times 10^8\,cm^{-2}$. The simultaneously measured CTE of the shielded channels is shown for comparison. An irradiation induced CTE minimum at a temperature of about 120 K, and an irradiation independent CTE minimum around 190 K were observed. The Mn-K flux was about 500 photons/cm^2 s and the transfer storage time Δt_s was reduced to 100 ns. The CTE improvement with integration time Δt_i = 76 ms and 765 ms respectively, is shown at the temperature of 120 K.

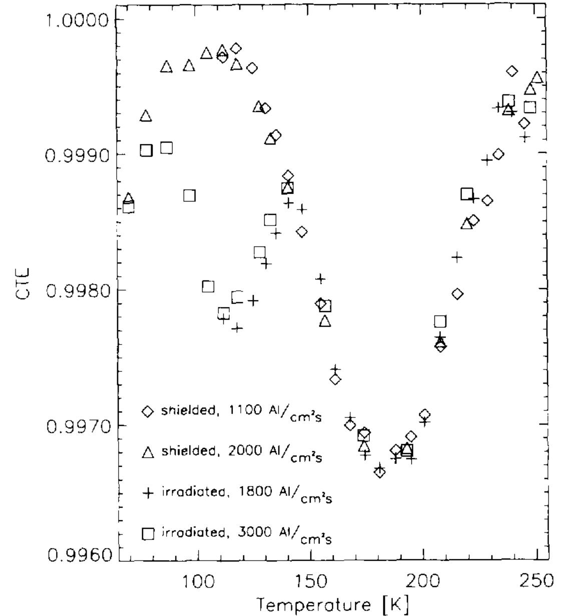

Fig. 9. Temperature scan of pn-CCD C6-21-12 with Al-K_α X-rays (1486 eV). The relative charge loss (CTI) is higher but the absolute charge loss is lower than for Mn-K_α X-rays (Fig. 8) for similar operating conditions.

(once per row) and the integration time (once per image = 60 rows). The charge loss improvements by reducing Δt_s from 900 ns (Fig. 11) to 100 ns, are shown in Fig. 12.

A further shortening of Δt_s to 50 ns (limit without degrading the pulse shape) and Δt_r from 64 μs to 22.5 μs resulted in small CTE improvements only.

An increase of the integration time Δt_i by a factor of ten has a favourable effect on CTE (see Fig. 8, T = 120 K).

2.2.7. Energy resolution

The Mn-$K_{\alpha,\beta}$ spectrum shows no significant degradation even for proton fluences of $1.5 \times 10^9\,cm^{-2}$ [15]. This was observed for not too low temperatures, e.g. 150 K, and by the usage of a CTE correction according to Eq. (2).

3. Monte Carlo simulation model of trap dependent charge transfer

A comprehensive Monte Carlo simulation model was developed to calculate the trap dependent charge transfer in a pn-CCD in detail. The model is based on the capture and emission times due to the Shockley–Read–Hall theory (Eqs. (3)–(5)). All parameters can be considered as

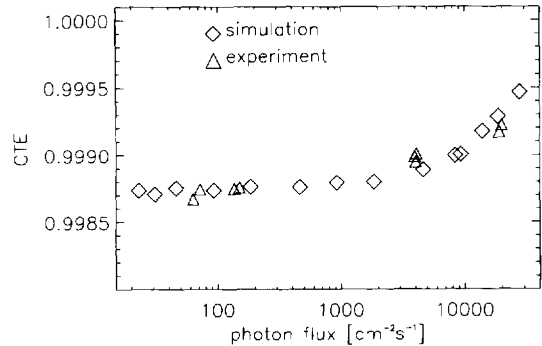

Fig. 10. CTE dependence on photon flux at T = 120 K for pn-CCD C6-21-12. For the Monte Carlo simulation the same trap energy level, capture cross section and entropy change factor are used as in Fig. 14. The trap concentration N_t of $9 \times 10^9\,cm^{-3}$ is adapted to the lower proton exposure of this pn-CCD. The results of the Monte Carlo simulations are very close to the measured CTE values. The emission time constant $\tau_e \approx 100$ μs is slightly longer than the sum of readout and transfer time of a pixel (64 μs). The electrons are however trapped more than one time on their way to the anode. An increase in Cu-K flux reduces the time between transferred signal charge packets and therefore the concentration of empty traps. Because of the short emission time constant the CTE improvement occurs especially for high proton fluxes.

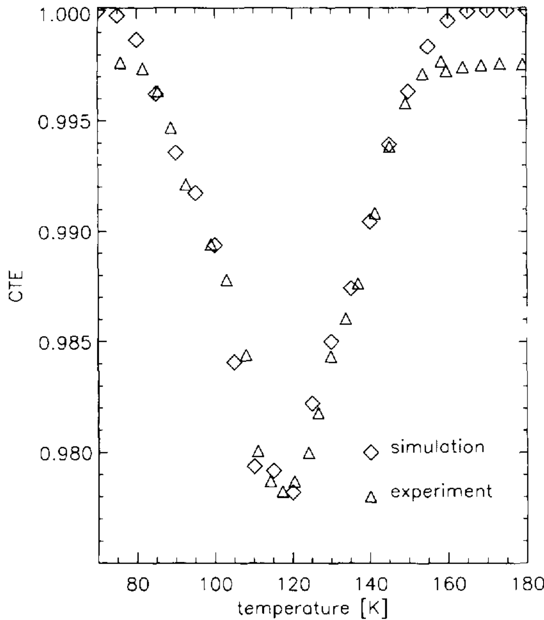

Fig. 11. Temperature scan with a long storage time during transfer $\Delta t_s = 900$ ns. For the Monte Carlo simulation is only one trap type assumed with $E_t = E_c - 0.17$ eV, $\sigma_c = 1 \times 10^{-14}$ cm^2, $X_n = 0.5$ and $N_t = 6.8 \times 10^{10}$ cm^{-3}. The long storage time causes a high capture probability but also a high reemission probability into the charge packet. We observe therefore a steep trailing and leading edge in the scan.

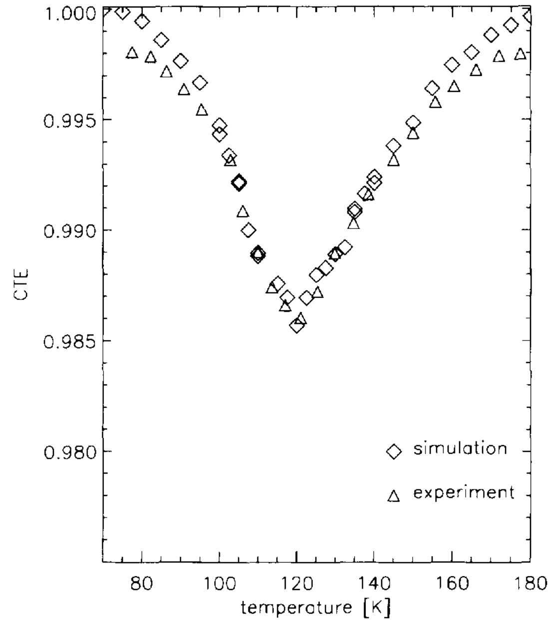

Fig. 12. Experimental CTE temperature scan with a reduced storage time $\Delta t_s = 100$ ns instead of 900 ns (Fig. 11). The change of this timing parameter is taken into account in the Monte Carlo simulation. Its results are shown in the figure too. Again the curves are corresponding well. The reduction of charge losses is simply caused by the shorter time for traps to capture signal electrons. The temperature where the CTE minimum occurs remains unchanged compared to Fig. 11.

constant for a sufficiently small time interval Δt. Empty traps have a small probability to be occupied, and occupied traps to be depopulated during Δt. In Fig. 13 is a scheme shown of the CTE determining parameters in the simulation.

3.1. Input

- temperature,
- pn-CCD: Gaussian distribution of electron density in storage potentials[2],
  timing scheme (sequence of storage times Δ_i, Δ_r, Δ_s),
  time interval Δt ($\ll$storage times Δ_i, Δ_r, Δ_s),
  transfer channel: number of pixels,
  dark current,
- trap: energy level $E_c - E_t$,
  capture cross section σ_c,
  entropy change factor X_n,
  concentration N_t,
  presence of several trap types simultaneously,
  random uniform local distribution,
- X-ray photons: energy,
  flux.

Only the traps in the storage regions are taken into account for trapping (see Section 1.4). We start with an electron occupation of all traps.

3.2. Main programme

The X-ray photons illuminate the detector during the integration time. Their number is calculated by the photon flux, the time and the area of a transfer channel. They are randomly distributed to the pixels of the transfer channel. The quantity of generated electrons is calculated by the ratio of photon energy and the average electron–hole creation energy in silicon (3.65 eV). Electron capture and electron emission is simulated during each time interval Δt (see below). If the chosen time interval Δt is sufficiently small – much smaller than the storage times – the capture and emission process becomes approximately continuous without large changes in the number of occupied traps and free electrons. This is the requirement for the separation of

[2] The electric potentials of the pn-CCD are simulated with TOSCA programme code [4]. The Gaussian distribution of electron density is due to the approximately parabolic shape of the storage potentials. The standard deviation of the Gaussian distribution is larger for charge storage at the shift registers $\varphi 1$, $\varphi 2$, $\varphi 3$ than between them, according to the TOSCA simulations (Fig. 2).

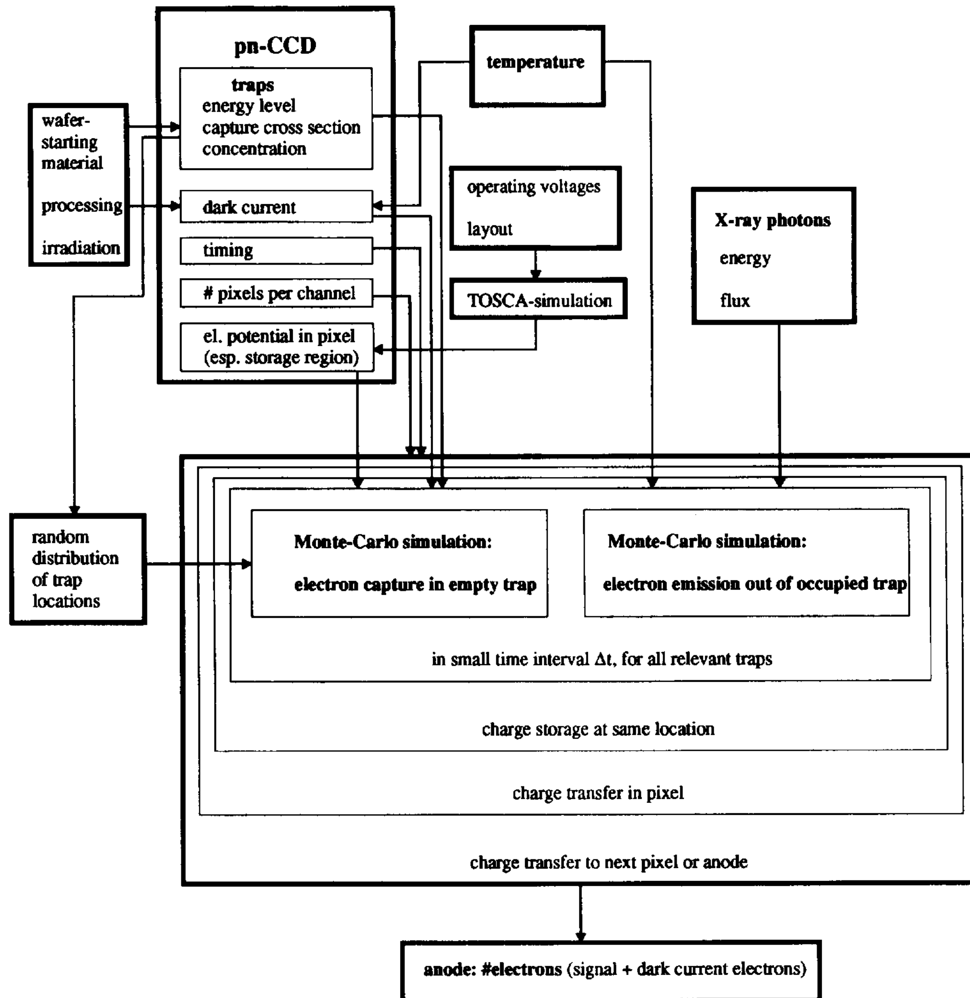

Fig. 13. Scheme of the CTE determining parameters in the Monte Carlo simulation model. The simulation programme was developed to describe the trap dependent charge transfer in a pn-CCD in detail. It is based on the capture and emission times of traps according to the Shockley–Read–Hall theory. The input parameters for the simulations are the energy levels, capture cross sections, entropy change factors and concentrations of the trap types; the temperature, the electric potentials, the dark current in the bulk, the timing scheme of the pn-CCD and the energy and flux of the X-ray photons.

electron capture and emission in a storage region. The number of dark current electrons per pixel which is generated during this time interval, is added to the number of free electrons in the storage region.

The occupation state of each trap and the number of free electrons is updated for the next time interval due to the processes in the previous time interval.

This procedure has to be applied to each time interval Δt. A transfer to the next storage region is considered in the sequence of the time intervals Δt according to the timing scheme of the pn-CCD. After one cycle time Δt_c all pixels are read out and the next cycle starts again with the integration time, and so on.

3.3. Electron capture during time interval Δt

For all empty traps in the current storage region of each pixel: With the current number of free electrons in each storage potential we get the electron densities $n_s(x, y, z)$ at the trap positions (x, y, z). The capture time constant τ_c is obtained then according to Eq. (4). The capture probability for each empty trap results in:

$$P_c(\Delta t, x, y, z) = 1 - \exp\left(-\frac{\Delta t}{\tau_c(x, y, z)}\right). \quad (6)$$

For sufficiently small time intervals Δt we achieve:

$P_c(\Delta t, x, y, z) \ll 1$. Random numbers (uniform deviate) $0 \leq R \leq 1$ are generated and compared with the capture probability $P_c(\Delta t, x, y, z)$ for each trap. If $R \leq P_c(\Delta t, x, y, z)$ the originally empty trap is occupied by an electron and the number of free electrons is reduced by one.

3.4. Electron emission during time interval Δt

For all occupied traps in the six storage regions of each pixel, the emission probability is given in the same way by:

$$P_e(\Delta t) = 1 - \exp\left(-\frac{\Delta t}{\tau_e}\right). \qquad (7)$$

For sufficiently small time intervals Δt one has again: $P_e(\Delta t) \ll 1$. Random numbers (uniform deviate) $0 \leq R \leq 1$ are generated and compared with the emission probability $P_e(\Delta t)$ for each trap. If $R \leq P_e(\Delta t)$ the originally filled trap is emptied. The released electron is assigned to a storage region, according to the present electric field configuration. The number of free electrons is increased there by one.

3.5. Output

The number of transferred electrons is obtained for each pixel. After subtraction of dark current offset which is generated during the cycle time, the signal amplitudes are determined. Finally the CTE is calculated according to Eq. (2).

The first cycles are rejected due to the arbitrary starting condition for the trap occupation. The accuracy of the CTE determination increases with the number of simulated cycles.

3.6. Special features of the Monte Carlo simulation

The simulation model includes the possibility that a trap can capture and release an electron in the same storage region several times. This is in particular probable during the long integration time of tens of milliseconds.

Furthermore repeated capture of an electron in traps of successive storage locations can occur on its path towards the anode.

For low photon fluxes, the average number of photons per transfer channel and cycle time can be smaller than one. In this case it is simulated that a photon is only incident at each n-th ($n = 2, 3, 4, \ldots$) cycle.

4. Analysis of experimental results

The dominant (irradiation induced) defect type is studied in this section with the Monte Carlo simulations described above. The simulations are compared with the measurements for different trap parameters $E_c - E_t$, σ_c, X_n, N_t. Finally a set of parameters was obtained which describes the measurements well: $E_c - E_t = 0.17$ eV, $\sigma_c = 1 \times 10^{-14}$ cm^2, $X_n = 0.5$. The trap concentrations N_t of the devices are shown in Table 2. The other input parameters for the simulations were chosen as in the measurements (temperature, timing, photon energy and flux, etc.).

4.1. Scatterplot

Fig. 14 shows a scatterplot calculated by the Monte Carlo simulation program. The results are very close to the corresponding measurements of Fig. 6. The upper curve shows the signals of the leading pixel, the two lower lines describe the collected electrons after trapping and detrapping in the first and second successive pixels. The steep tail of a single transferred signal charge packet can be seen in the Monte Carlo simulation of Fig. 15. The emission time constant τ_e is about 30 μs. The storage times are: $\Delta t_i = 63$ ms, $\Delta t_r = 60$ μs and $\Delta t_s = 900$ ns. The length of the signal tail increases with an increasing number of pixel transfers. This is caused by repeated capture and emission of signal electrons during the transfer.

In the satellite mission, only signals are sent to earth which exceed the signal detection threshold. This has to be done to reduce the telemetry rate. As threshold is a value applied of a few times the standard deviation of noise which is about five electrons. The whole signal tail can be fitted with the Monte Carlo simulations. The total photon

Table 2
Dependence of A-centre generation on proton exposure. The concentrations were obtained with the Monte Carlo simulations. The fluctuation of the trap concentrations obtained by the simulations, is small compared to the results got by DLTS measurements.

CCD-id	Proton fluence [cm^{-2}]	$\Delta E/p$ [MeV]	A-centre concentration [cm^{-3}]	A-centre/proton
C6-21-12	6.0×10^8	2.4	$0.5–0.9 \times 10^{10}$	0.2–0.4
C6-21-3	1.5×10^9	2.4	1.4×10^{10}	0.2
C6-28-3	2.6×10^9	2.4	($<6.8 \times 10^{10}$)	(<0.7)
C6-23-12	6.5×10^9	3.3	6.8×10^{10}	0.3

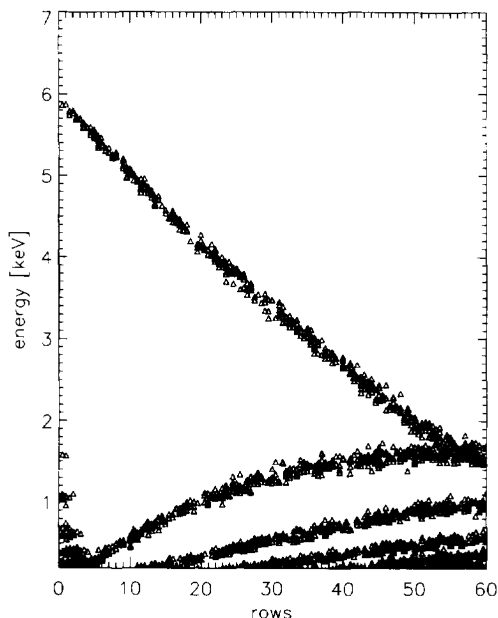

Fig. 14. The shown scatterplot was generated by the Monte Carlo simulations. The experimental operating conditions were used as input. With the trapping parameters $E_t = E_c - 0.17$ eV, $\sigma_c = 1 \times 10^{-14}$ cm^2, $X_n = 0.5$ and $N_t = 6.8 \times 10^{10}$ cm^{-3} we obtained the same results as in the measurements (see Fig. 6).

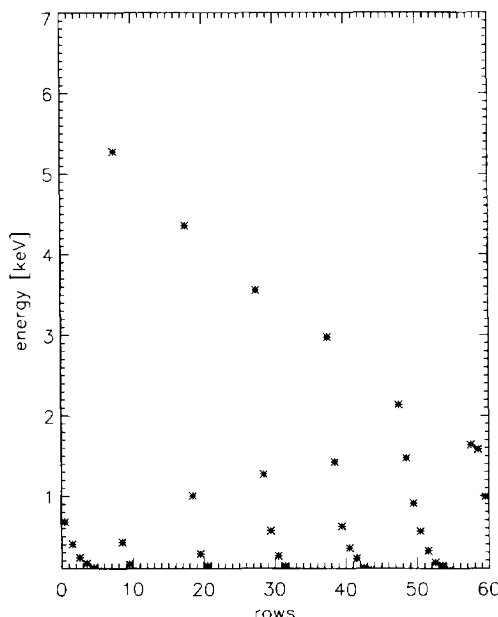

Fig. 15. The picture shows the signal tails of photons which are hitting selected pixels of Fig. 14. The shape of the tails reflects the short emission time constant τ_e. The photon with incidence in pixel #58, close to the end of the transfer channel, continues its tail in the first pixels of the next image.

energy can be reconstructed then by summing up the signal amplitudes in the successive pixels. This is important for long emission times, i.e. low temperatures, with far ranging signal tails.

4.2. CTE dependence on temperature

The temperature dependent effect of a trap type on CTE can be understood using Eq. (5) only. For low temperature, the emission time is much longer than the time between two successive transferred charge packets (see Fig. 5). The number of empty traps is then significantly reduced. As a result the CTE is high.

With increasing temperature the emission time is reduced. The number of unoccupied traps is then increased and the CTE values fall.

Finally a temperature is achieved at which all occupied traps are emptied before the next signal charge packet is transferred. The Monte Carlo simulations of the experimental temperature scans have shown that the CTE minimum occurs at a temperature, at which the emission time ($\tau_e \approx 100$ μs) is only slightly longer than the time needed for a pixel (or row) transfer and readout: $5 \times \Delta t_s + \Delta t_r \approx 65$ μs. With further increase of temperature the emission time becomes so short that trapped signal electrons are released in time to join again the charge packet. For this reason CTE increases with temperature. In addition, for temperatures higher than 200 K, the increasing leakage current fills a non-negligible fraction of traps.

Accordingly, every trap type generates a CTE valley in a temperature scan. The position in temperature of the CTE minimum depends mainly on the energy level of the trap. The emission time constant τ_e of a shallow trap level $E_c - E_t$ at a low temperature is the same as for a deep trap level at a higher temperature due to Eq. (5). This is valid with the assumption of similar capture cross sections for the two trap types. Thereby the CTE minimum occurs for a shallow trap at a lower temperature than for a deep trap level.

The temperature dependence of CTE on the described trap type is shown in Fig. 11. At temperatures below 80 K and above 150 K, CTE is no more depicted by this defect type only. The charge losses result then from a superposition with other trap types. One has a very shallow energy level and decreased the CTE for temperatures lower than 100 K (see Fig. 17). The minimum is still not reached, even at a temperature of 60 K. At temperatures above 150 K, a trap type with a deep energy level limits the CTE.

4.3. CTE dependence on proton fluence

The defect formation was observed to be dependent on the proton fluence. From a comparison of the experimental and simulated CTE scans versus temperature we obtain the trap concentration. Their values N_t are presented in Table 2 for the different proton exposures of the pn-CCDs. We

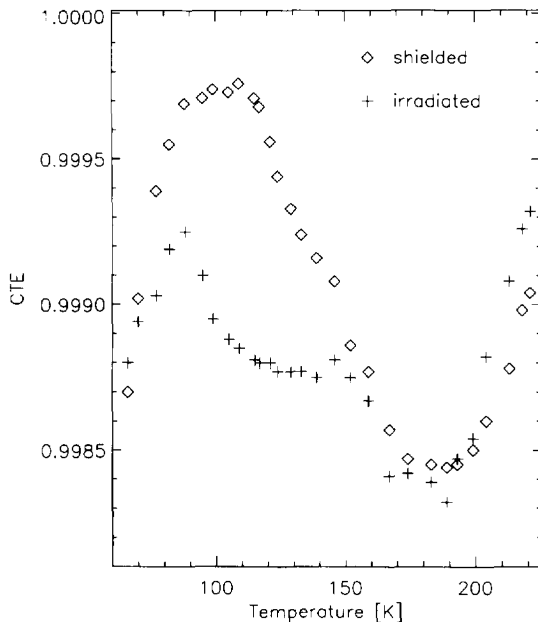

Fig. 16. Comparison of CTE for irradiated and shielded channels of pn-CCD C6-21-12 after thermal annealing at 270°C for 4 hours. The irradiation induced CTE-minimum is already slightly recovered compared to measurements with the same device, presented in Fig. 8.

observe a defect formation proportional to the proton fluence.

4.4. CTE dependence on photon energy

We have observed that the absolute loss of electrons is only slightly reduced at lower X-ray energy (see Figs. 8, 9). We conclude from Eqs. (4) and (6) that the capture probability P_c decreases with the electron density n_s. For a sufficiently long storage time, the capture probability remains high and the charge loss is more dependent on the number of traps in the storage region. The relative charge losses (CTI) increase thereby with lower photon energy (see Figs. 8, 9).

4.5. CTE dependence on photon flux

The Monte Carlo simulation of CTE dependence on photon flux is shown in Fig. 10. The concentration of empty traps is reduced for the storage regions which the signal charges pass towards the anode. The emission time constant $\tau_e \approx 100\,\mu s$ at the temperature of 120 K is only slightly longer than the transfer and readout time for a pixel (≈65 μs). The effect of trap occupation in the transfer channel lasts longer than the emission time. This is caused by repeated capture of the signal electrons in successive pixels. Therefore the CTE is already appreciably increased for the photon fluxes shown in Fig. 10 with a not too low density of signals in the transfer channel.

4.6. CTE dependence on storage time

The simulation of storage time Δt_s reduction from 900 ns to 100 ns is shown in Fig. 11 and Fig. 12. The experimental values are represented in the figures too. The CTE improvement is due to the smaller capture probability of electrons in traps.

The signal packet density in the pn-CCD increases with integration time for a given photon flux (see Fig. 8, $T = 120$ K). The rise in CTE occurs therefore due to the same reason as for the higher photon flux.

5. Defect identification

Three different trap types were observed in the Transfer Efficiency measurements. The main, radiation induced defect type discussed above, has been identified. The other two trap types are still under study.

5.1. Main defect type: A-centre

This defect type was analyzed with several methods:

1) Charge Transfer Efficiency Measurements and Monte Carlo Simulations. The Monte Carlo simulations fit well together with the experimental results for a trap type with an energy level of $E_t = E_c - 0.17$ eV and a temperature independent capture cross section of 1×10^{-14} cm^2. These parameters are very similar to those observed for a vacancy-oxygen$^{(0/-)}$ defect complex with conventional methods like DLTS, TSC, TSCAP, etc. For its energy level the following values were obtained: $E_t = E_c - 0.169$ eV, 0.17 eV and 0.174 eV respectively [6,9,16] and for the temperature independent capture cross section: $\sigma_c = 1 \times 10^{-14}$ cm^2. This kind of defect is called A-centre. It is generally observed after particle irradiation of silicon. An entropy change factor X_n of 0.5 for A-centres, given by Brotherton et al. [6], was used for the simulations. The measurements (Figs. 8, 9) show that CTE of the shielded channels reaches the highest values in the temperature scan between 110 K and 120 K. Therefore we conclude that the concentration of A-centres is negligible before irradiation.

2) DLTS analysis. Deep Level Transient Spectroscopy (DLTS) measurements of diodes fabricated and irradiated together with the pn-CCDs were carried out at the University of Erlangen, Germany, and at IMEC, Belgium [17]. Both groups found independent of each other, a defect type which is induced by irradiation. A mean energy level of about $E_t = E_c - 0.17$ eV and a capture cross section σ_c of approximately 1×10^{-14} cm^2 were observed. This confirms the Monte Carlo simulation results. The concentrations evaluated with DLTS are not very accurate because they are close to the detection limit of the method.

The same results $E_t - E_c = 0.17$ eV, $\sigma_c = 1 \times 10^{-14}$ cm^2 were obtained by DLTS measurements of Fretwurst et al. [18] after neutron irradiation of devices fabricated by our semiconductor laboratory.

3) Annealing experiment. After a thermal annealing of the pn-CCD C6-21-12 up to a temperature of 270°C we observed only small improvements of the degraded CTE (see Fig. 16). A complete annealing of the irradiation induced defect type occurred however at a temperature of 350°C (see Fig. 17). This fits well to the high annealing temperature for A-centres of about 300–350°C [6,16].

5.2. Deep level defect: $E_c - E_t = 0.3$ eV

The second CTE minimum around 190 K is caused by a trap level $E_c - E_t$ of about 0.3 eV (analyzed with DLTS measurements, Monte Carlo simulations, [2,19]). The CTE is appreciably degraded after irradiation only for the pn-CCD C6-23-12 at this temperature (see Fig. 7). The transfer losses of Mn-K$_\alpha$ photons were about a factor of 2 higher compared to the shielded channels in this device. It has been exposed to the highest proton fluence of 6.5×10^9 cm^{-2}. In addition, the proton energy deposition in the detector after passage through a thicker scattering foil was higher than in the other runs (see Table 1).

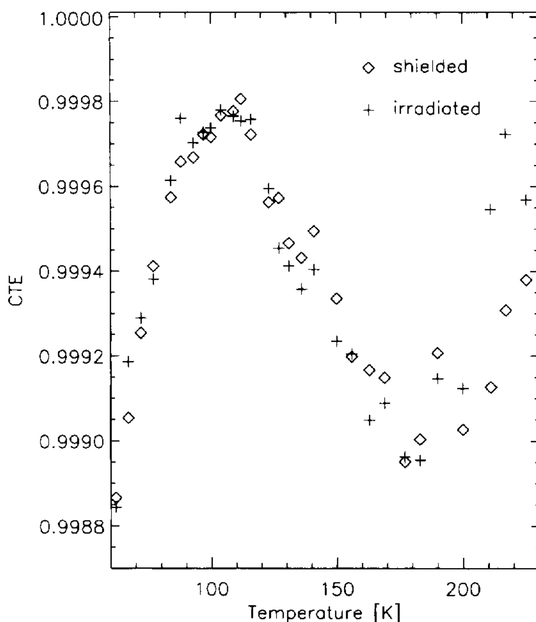

Fig. 17. Comparison of CTE for irradiated and shielded channels after thermal annealing at 350°C for 4 hours. A total recovery of CTE was achieved at this temperature. This confirms the identification of the irradiation induced defects as A-centres. The second trap type causing the CTE minimum at 190 K, remained unchanged by the annealing experiment. The same was observed for the CTE degradation below the temperature of 100 K.

A trap with an energy level $E_c - E_t = 0.30$ eV was also observed in proton irradiated MOS-CCDs by A. Holland [12]. It was obtained with an analytical steady-state model for CTI. In contrast to our measurements, the concentration of the trap was increased by a factor of 10 after 10 MeV-proton irradiation with a fluence of 3.6×10^9 cm^{-2}. The temperature of CTE degradation occurrence was about the same in the MOS-CCDs compared to our devices.

5.3. Shallow level defect: $E_c - E_t \leq 0.08$ eV

A proton exposure independent CTE degradation could be observed at very low temperatures. The corresponding CTE minimum is not reached even at a temperature of 60 K (see Fig. 17). DLTS measurements and the Monte Carlo simulations revealed a very shallow trap with an energy level of $E_c - 0.05\text{ eV} \leq E_t \leq E_c - 0.08$ eV.

A similar energy level of 0.06 eV was also observed by Fretwurst et al. [18] in non-irradiated silicon diodes.

5.4. E-centre and divacancy

The DLTS measurements of the diodes detected also an energy level of 0.42 eV and a capture cross section of about 1×10^{-15} cm^2 after exposure to high proton fluences. The origin of the trap could be the E-centre (P–V)$^{(0/-)}$ with $E_c - E_t = 0.456$ eV (0.40–0.47 eV), $\sigma_c = 3.7 \times 10^{-15}$ cm^2. Another possibility is the divacancy$^{(0/-)}$ with two levels $E_c - E_t = 0.39$ eV and 0.41 eV and the corresponding capture cross sections of $\sigma_c = 4 \times 10^{-15}$ cm^2 and 2×10^{-15} cm^2 respectively [6,11,16,20–22]. Both defect types are often seen in proton or electron irradiated silicon.

5.5. E-centre

The concentration of E-centres in our pn-CCDs can be estimated due to the results of Su et al. [23]. The ratio of A-centres (O–V) to E-centres (P–V) is approximately 0.072 times the ratio of the concentrations of oxygen and phosphorus atoms. In the depth of charge transfer we have about 1×10^{16} cm^{-3} oxygen atoms [17] and 1×10^{14} cm^{-3} phosphorus atoms. This leads to a factor of 7 less E-centres than A-centres. Furthermore the capture cross section of E-centres is about a factor of 3 smaller than that of A-centres.

5.6. Divacancy

In the order of ten vacancies per 10 MeV proton are generated in the detector ([24], TRIM90 calculation [14]). They can be captured by oxygen and phosphorus atoms. Furthermore a diffusion of vacancies to the surface of the device occurs. For these reasons we expect a relatively low probability for interaction of vacancies. Therefore the

concentration of divacancies in the silicon bulk is low. In addition, the capture cross section and accordingly the capture probability of a trap is smaller than that of A-centres.

The trap parameters detected with DLTS (with the assumption of a temperature independent capture cross section and an entropy change factor of one) were used as input for a Monte Carlo simulation. The corresponding CTE minimum would occur far above 200 K for the used timing scheme to operate the pn-CCD. But no significant effect could be observed in the experimental temperature scan up to a temperature of 240 K. The number of thermally stimulated electrons increases with the temperature. The resulting occupations of traps could hide the trapping effects of these defect types at the relatively high temperatures.

The divacancy occurs in another charge state $V\text{–}V^{(-/=)}$. Its corresponding energy level is $E_c - 0.23$ eV; because of the Coulomb repulsion the temperature dependent capture cross section $\sigma_c = 4 \times 10^{-16} \exp(-0.017/kT)\,\text{cm}^2$ [6,21], is smaller than in the other charge state $V\text{–}V^{(0/-)}$. The CTE minimum should occur at a temperature of about 170 K (Monte Carlo simulations). The comparison of shielded and irradiated channels however, shows no appreciable deterioration of CTE after proton exposure at this temperature. This confirms the low concentration of divacancies.

Due to the lower concentration, the smaller capture cross section and a trap occupation by thermally stimulated electrons, it is understandable to observe no significant effect of the E-centre or divacancy on charge transfer, in contrast to that of the A-centre.

The DLTS method is applied for defect analysis. The time to fill the traps and a sufficiently high electron density are chosen for that purpose. For this reason the trap with $E_c - E_t = 0.42$ eV was detected in the DLTS measurements but not in our studies of Charge Transfer Efficiency.

5.7. Annealing

A thermal annealing up to a temperature of 350°C had no significant effect on the concentrations of the traps with energy levels of 0.05–0.08 eV and around 0.3 eV. This proves again that there is no correlation between charge transfer degradation and the E-centre or divacancy which have annealing temperatures of 150°C and 300°C respectively [6,10,11,16,20].

For identification of these defect types their energy levels and capture cross sections has to be measured more accurately. A timing scheme with long storage times (especially $\Delta t_s \gg \mu$s) which results in high charge losses, has to be applied for that. In addition, a higher proton exposure would be useful to study the defect around 190 K. This would also facilitate the observation of E-centre and divacancy effects on charge transfer.

6. Conclusions

The radiation hardness of the pn-CCD detector was tested and fulfills the requirements for the expected proton radiation environment and operating temperatures (140–190 K). A significant increase in charge transfer losses was found for low temperatures around 120 K. An operating temperature of at least 140 K can be recommended for the pn-CCD EPIC detector on the XMM satellite mission.

The temperature, timing scheme, photon flux and energy dependence of the Charge Transfer Efficiency shows that it is mainly caused by trapping centres. The Monte Carlo simulation model was used for defect identification and for a study of the effect of traps on charge transfer.

An energy level of $E_c - E_t = 0.17$ eV and a capture cross section of $\sigma_c = 1 \times 10^{-14}\,\text{cm}^2$ was observed. The dominant irradiation induced trap type was identified as A-centre, an oxygen-vacancy defect in the silicon lattice.

This was confirmed by annealing experiments and Deep Level Transient Spectroscopy measurements. The A-centre concentration increases proportional to the proton fluence.

A second CTE degradation occurring in the non-irradiated pn-CCDs around 190 K, is hardly proton exposure dependent.

6.1. Further methods for CTE improvement

Several ideas have been proposed to improve the CTE. This reduces signal loss corrections, decreases the number of calibration measurements and lowers transfer noise. Furthermore CTE will be more independent on radiation damage.

1) Narrowing of transfer channel

To reduce the number of traps which the signal electrons will see on their way to the anode, the transfer channel width must be reduced. This was achieved in a newer pn-CCD fabrication by an additional small phosphorus implant along the transfer channel. The first results of narrowing the transfer channel width were obtained for unirradiated pn-CCDs of fabrication #7. The transfer losses are reduced then by a factor of 5 [2]. A test of proton irradiated devices will follow in the near future.

2) Trap saturation

A saturation of traps can be obtained by illumination of the device or electron injection. This method, called fat zero, has to be done quickly before an image is taken. Charge losses during the transfer can be significantly decreased then. However this works most effectively for traps with an emission time much longer than the time needed for taking one image (tens of milliseconds). Assuming an operating temperature of 140 K for XMM the emission time constant τ_e is approximately 5 μs for A-centres. Therefore no CTE improvement would be expected for that defect type. For the preirradiation induced defect type with $E_c - E_t \approx 0.3$ eV ($\tau_e \approx 1$ s), the divacancy

with $E_e - E_t = 0.39$ eV and 0.41 eV and the E-centre with a deep energy level of $E_c - E_t = 0.46$ eV, the CTE will be improved.

3) Oxygen concentration

The formation probability of A-centres increases with the oxygen concentration. For this reason, the amount of oxygen in the silicon wafer substrate material should be specified.

For low operating temperatures of about 120 K or very high irradiation exposures the oxygen concentration should be kept as low as possible.

If the detector should be operated at temperatures above 200 K it is desirable to have a high oxygen concentration. The getter effect of oxygen atoms for generated vacancies can be used to keep the formation probability of phosphorus-vacancy defects and divacancies small.

The main detectable impurity concentrations should be specified too for the silicon wafer supplier to prevent undesirable changes in trap concentrations for different detector fabrications.

Acknowledgements

We thank W. Dünnweber for his support at the TANDEM accelerator in Garching, P. Solc for the mounting and bonding of the devices, R. Richter for his TOSCA simulations of the electric potentials in the pn-CCD.

The project was supported by the Deutsche Agentur für Raumfahrtangelegenheiten (DARA) under contract No. 50 0X 93025/-XMM-EPIC and by the EUROPEAN SPACE AGENCY under contract No. 8873/90/NL/PB(SC) CCN No. 1

References

[1] H. Bräuninger et al., Nucl. Instr. and Meth. A 326 (1993) 129.
[2] H. Soltau et al., these Proceedings (7th Europ. Symp. on Semiconductor Detectors, Schloss Elmau, Bavaria, Germany, 1995) Nucl. Instr. and Meth. A. 377 (1996) 340.
[3] L. Strüder et al., Nucl. Instr. and Meth. A 288 (1990) 227.
[4] H. Gajewski et al., TOSCA Handbuch, Institut für Angewandte Analysis und Stochastik (IAAS), Karl Weierstraß-Institut, Berlin, 1992.
[5] J.D.E. Beynon and D.R. Lamb, Charge-Coupled Devices and Their Applications (McGraw-Hill, 1980) p. 59.
[6] S.D. Brotherton and P. Bradley, J. Appl. Phys. 53 (1982) 5720.
[7] E. Banghart et al., IEEE Trans. Electron Devices ED-38 (5) (1991) 1165.
[8] A. Mohsen and M. Tompsett, IEEE Trans. Electron Devices ED-21 (11) (1974) 701.
[9] Landolt-Börnstein, III/22b, Semiconductors: Impurities and Defects in Group IV Elements and III–V Compounds (Springer, 1989) pp. 65, 69.
[10] D. Bräunig, Wirkung hochenergetischer Strahlung auf Halbleiterbauelemente (Springer, 1989) pp. 40, 45.
[11] M.S. Robbins, Radiation Damage Effects in Charge Coupled Devices, Brunel University, Uxbridge, Middlesex, UK, Ph.D. dissertation (1992) p. 107.
[12] A.D. Holland, Nucl. Instr. and Meth. A 326 (1993) 335.
[13] G.R. Hopkinson, CCD Radiation Damage Study, European Space Agency Contract Report, No. 9557/91/NL/LC(SC), 1995.
[14] TRIM90, Transport of ions in matter, described in: The Stopping and Range of Ions in Silicon, J.F. Ziegler, J.P. Biersack and U. Littmark, Vol. 1 (Pergamon, 1985).
[15] N. Meidinger et al., IEEE Trans. Nucl. Sci. NS-42 (6) (1995) 2066.
[16] J.W. Walker and C.T. Sah, Phys. Rev. B 7 (1973) 4587.
[17] IMEC, Technical Note Related to CCN-01/C00-17, Investigation of MPE Material and Devices, 1995.
[18] E. Fretwurst et al., Ref. [2], p. 258.
[19] N. Krause, Analyse und Optimierung der Ladungstransferverluste in volldepletierten pn-CCDs, Diplomarbeit, Technische Universität München, March 1996.
[20] G.R. Hopkinson, Proton Radiation Testing of CCDs for the SILEX Programme, European Space Agency Contract Report, No. 103607, 1991.
[21] A.R. Peaker and S. Guimaries, Properties of Silicon, EMIS Datareviews Series No. 4, INSPEC, Chap. 10.2, 1988.
[22] O.O. Awadelkarim et al., Phys. Status Solidi A 120 (1990) 539.
[23] Z. Su, A. Husain and J.W. Farmer, J. Appl. Phys. 67 (1989) 1903.
[24] E.A. Burke, IEEE Trans. Nucl. Sci. NS-33 (6) (1986) 2066.